

## Research Article

# Seismic Performance Evaluation of Double-Skin Semi-Base-Isolated Building Using Incremental Dynamic Analysis

Mohammad Parsaeimaram <sup>1</sup>, Congqi Fang <sup>1,2</sup>, Xianqi Luo <sup>1</sup> and Chandan Shakya <sup>1</sup>

<sup>1</sup>Department of Civil Engineering, Shanghai Jiao Tong University, Shanghai 200240, China

<sup>2</sup>School of Civil Engineering, Shanghai Normal University, Haisi Road No. 100, Shanghai 201418, China

Correspondence should be addressed to Congqi Fang; [congqifang@msn.com](mailto:congqifang@msn.com)

Received 10 October 2017; Revised 29 March 2018; Accepted 17 April 2018; Published 6 June 2018

Academic Editor: Alessandro Palmeri

Copyright © 2018 Mohammad Parsaeimaram et al. This is an open access article distributed under the Creative Commons Attribution License, which permits unrestricted use, distribution, and reproduction in any medium, provided the original work is properly cited.

Base isolation is a widely accepted earthquake damage prevention technique. This method decouples the superstructure from the base by putting a flexible layer under each column, thereby elongating the time period of structures. Semi-base isolation (SBI) in double-skin structures is an effective technique to reduce the dynamic responses of structures due to earthquake motions, by utilizing the isolation devices in part of it instead of the entire base. This study presents a double-skin structure consisting of outer fixed base frames with shear walls that have been detached from the inner core with a minor gap. The inner core of the structure has been dissociated from the base using the elastomeric bearings. Seismic response of 10-story double-skin structure with inner isolated core was compared to that of inner fixed base core to consider the yielding and collapse probability of the structure using the incremental dynamic analyses (IDA). The results showed that the time period in SBI buildings can be adjusted with the use of coupling beams between the inner and outer frames. Also, the time period and interstory drift ratio are both reduced as more floors are given coupling beams. However, these coupling beams are the most effective at the topmost floors.

## 1. Introduction

Seismic isolation is a design concept to dissociate the superstructure from its foundations completely or partially. Base isolation is an option to conventional structural design with fixed base and can be cost-effective for buildings located in areas where a highly ground motion is likely to occur [1]. Conceptually, isolation systems minimize the earthquake responses of the superstructure by separating the building from the base. By lengthening the time period of the building using isolation systems, forces transmitted to the structure above the base are significantly reduced. In fact, buildings with prolonged time periods are subjected to lower seismic force and divert energy of the ground motion. In particular, high-energy seismic ground motions are diverted at higher mode frequencies [2, 3]. Energy dissipation capacity and lateral flexibility are the basic characteristics of an elastomeric isolation. Flexibility increases the time period of the structure, thereby reducing the earthquake force that has to be absorbed by the isolation system, while energy absorbing

capacity itself reduces the seismic energy and increases damping of the building [4, 5]. During this procedure, a large amount of transmitted earthquake motion is dissipated while an adequate stiffness of the isolation device has to be provided to protect the structural integrity.

Uplift and compression force result from the overturning action due to the lateral forces on the lateral force resisting system (LFRS). In some cases, the isolators may be located under the LFRS (e.g., shear walls and bracing). In particular, the connection of the isolator to the LFRS should be carefully considered with respect to the transfer of tensile and compressive forces to the isolator under the columns. Although the horizontal and vertical stiffness of the rubber bearing can significantly withstand the transmitted compressive forces, the tensile forces (uplift) can cause instability in the isolation system.

The effects of the vertical component of earthquake acceleration on a structure had received relatively less attention in the past. Zhou et al. [6] studied several vertical and 3D isolation systems on the modern nuclear facilities. Their

study consisted of a series of case study analysis of the modern nuclear power plant model to examine the benefits and challenges associated with 3D isolation, compared to that of the horizontal isolation. This study compared the performance of horizontal isolators alone with that of isolators capable of damping vertical frequencies and found that isolators having vertical frequencies under 3 Hz can effectively reduce the vertical responses for the studied nuclear power plant model.

Takahashi et al. [7] proposed a 3D seismic base isolation system in order to apply vertical and horizontal earthquake motions to an actual three-story building. In their proposed 3D seismic isolation, they used a device consisting of laminated rubber bearings as a horizontal isolation device and air springs as a vertical isolation device. The study showed that the vertical and horizontal maximum absolute acceleration drastically decreases with the use of 3D seismic base isolators under each supporting point.

Furthermore, 3D seismic isolation models have been developed in the past, by adding limited vertical isolation systems to particular portions of a horizontally isolated structure [8–12], and in these studies, it was found that vertical isolation systems could better protect the structure against the vertical component of the response. However, the studies stated above were restricted to the vertical component of excitation, and the uplift force behavior was limited to the effectiveness of the vertical component of the earthquake acceleration. Accounting for the uplift force due to overturning moment could have resulted in a different response of the isolated structures when compared to the vertical component of excitation alone. As previously stated, isolated structures have a longer fundamental time period due to a flexible layer between the base and superstructure. In addition, the base isolation system is appropriate for structures that possess short to medium heights and whose dominant modes are within a specific frequency range. However, in highly seismic zones and in structures with longer period components, it is difficult to build components flexible enough for the energy due to ground motion to be reflected [13].

The presented study proposes a double-skin structure called SBI building to address the aforementioned issues and to reduce the effectiveness of uplift in isolation devices due to LFRS. The proposed model consists of isolators in only the inner part of the structure, in which the LFRS is located only at the perimeter of the building with fixed base as outer frames, and in which the inner gravity columns (inner core) have been supported by isolators beneath the columns with sufficient separation from the outer frame. To avoid uplift in the isolation devices, LFRS is located in the outer frames with fixed bases. Furthermore, in this system, the inner core is connected to the outer frames in every floor level in order to increase the stiffness of the structure and to decrease fundamental time period.

Several research projects have been conducted to account for various cases of double-skin facade (DSF) buildings in which the lateral loads have been assigned to and are resisted by the primary building structure, while the exterior skin is employed as a curtain wall. For such cases,

a significant amount of studies were carried out by Bedon and Amadio [14–16] for the mitigation and enhancement of glass curtains under extreme loads based on the potential of special mechanical connectors inserted between the primary structure and exterior glazing facade. And also they investigated the behavior of a cable-supported glazing facade subjected to high- and medium-level air blast loads [17, 18].

Recently, a variety of studies have focused on the properties and applications of double-skin system regarding environmental conditions and energy saving [19–21], while little research exists on the seismic behavior of this system. Moon [22, 23] studied the structural capacities of the double-skin facade (DSF) systems in tall buildings with fixed base subjected to dynamic wind loads. Furthermore, Pipitone et al. [24] employed several layouts of double-skin facade (DSF) with mass dampers to reduce the seismic vibration in structures subjected to variety of earthquake excitations. They proposed an optimized design configuration of double-skin facade (DSF) based on numerical analysis. Fu and Zhang [25] also proposed an integrated control system to combine double-skin facade and mass dampers in buildings. They show that by motorizing the DFCs, energy efficiency can be improved, and their results indicate that mass damper systems can significantly reduce structural motions under earthquake excitation. In [26], the effect of distributed mass dampers in multistory double-skin facade building under a set of 20 earthquake excitations was investigated. They employed both genetic algorithms (GA) and particle swarm optimization (PSO) techniques to find the optimal design parameters for double-skin facade panels. It was concluded that double-skin facade panels can reduce the seismic response up to 35% of the uncontrolled case.

The aforementioned literature reviews have been carried out with a primary focus on the environmental applications and energy aspects and as a vibration absorber under earthquake excitation of the DSF system. In fact, no substantial studies on DSF structures focusing on the application of base isolation in the DSF systems could be found in the approachable references.

Here, the seismic response of 3D nonlinear finite element analysis of a double-skin semi-base-isolated (SBI) multistory building, composed of fixed base reinforced concrete (RC) frames with shear walls as outer frames and an inner isolated core with a sufficient gap from the outer frames, is investigated and the results are compared to that of inner fixed base core, under bidirectional earthquake acceleration. Incremental dynamic analyses (IDA) is used to estimate the performance of structures under seismic loading using OpenSees [27], for the modeling and analyses. Fragility functions of SBI and fixed base on the double-skin structures are generated and compared and the results obtained are discussed.

## 2. Structure and Model Description

The prototype reinforced concrete (RC) building presented herein is a 10-story double-skin structure with moment resisting connections. The typical floor plan and elevations of the structural models used in this study are illustrated in

Figure 1. The design of all buildings satisfy UBC-97 [28] and ACI 318-11 [29] requirements. Six prototype buildings are assumed to be located in seismic zone 3 on the stiff soil ( $S_D$ ) based on UBC-97 [28] classification. For the purposes of this study, four double-skin structures and two conventional structures with identical configurations were considered as described below and results were compared for better understanding.

The double-skin structures in consideration can be split into two parts, namely, inner core and outer frames. Among these, the outer frames were considered to be fixed. Furthermore, the two aforementioned conventional structures consist of the inner core of the double-skin structure which has been embedded with the inside of the exterior skin.

Each model is given a name, starting with the letters “IFBC” or “IIC” to represent inner fixed base core and inner isolated core, respectively, followed by numbers or with the word “All” to denote the floor number in the inner core that are connected to the outer frames with coupling beams as illustrated in Detail-2 of Figure 1. Detail-2 shows the connection of the beam element between the inner core and the outer frames.

Based on the above statements, six prototype models are defined as (IIC-10th), (IFBC-10th), (IIC-All), (IFBC-All), (IIC), and IFBC. Configurations of all the models are explained in the following:

- (i) Model IIC-10th stands for a double-skin structure with inner isolated core in which the inner core has been connected to the outer frames at the tenth-floor level, as illustrated in Figure 1(b).
- (ii) Model IFBC-10th stands for a double-skin structure with inner fixed base core in which the inner core has been connected to the outer frames at the tenth-floor level, as illustrated in Figure 1(c).
- (iii) Model IIC-All stands for a double-skin structure with inner isolated core in which the inner core has been connected to the outer frames at all floor levels.
- (iv) Model IFBC-All stands for a double-skin structure with inner fixed base core in which the inner core has been connected to the outer frames at all floor levels.
- (v) Model IIC stands for a structure with an inner isolated core only, which has no outer frames.
- (vi) Model IFBC stands for a structure with an inner fixed base core only, which has no outer frames.

Four RC shear walls are located in the outer frames in both longitudinal and transverse directions to withstand lateral earthquake forces. Moment resisting connections are used at the intersection of beams and columns. The cross sections of the beam elements in the inner core and outer frames are assumed to be equal in all stories. The plan view of the 10-story square buildings with three 4.0 m bays is depicted in Figure 1(a). All stories have typical heights equal to 3.0 meters. The dead and live loads are assumed to be  $6.50 \text{ kN/m}^2$  and  $2.50 \text{ kN/m}^2$ , respectively. The compressive strength of concrete is assumed to be 25 MPa, and the tensile

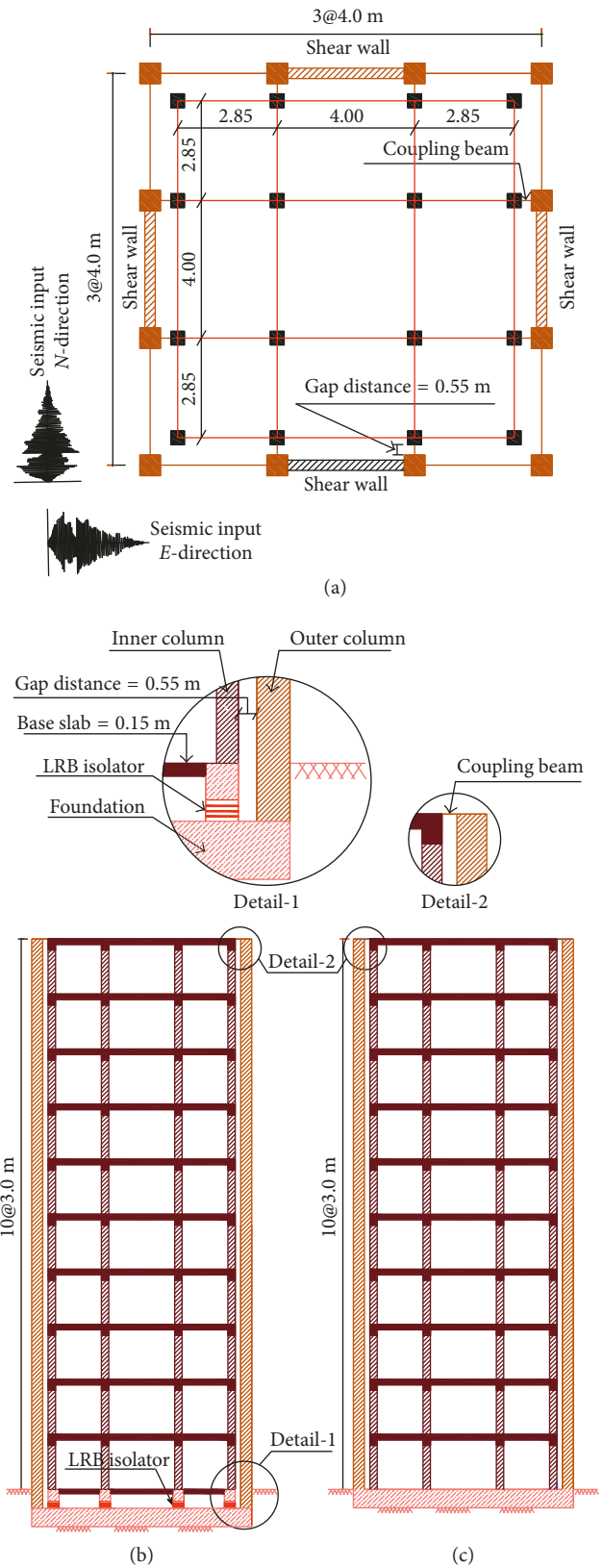


FIGURE 1: Structural model of buildings: (a) typical floor plan of the structural models, (b) inner isolated core with coupling beam elements at the tenth-floor level (IIC-10th), and (c) elevation of inner fixed base core with coupling beam elements at the tenth-floor level (IFBC-10th).

TABLE 1: Cross-sectional dimensions of structural elements.

Story	Outer elements			Inner elements	
	Column (mm)	Beam (mm)	Shear wall (mm)	Column (mm)	Beam (mm)
1–7	700 * 700	600 * 400	Thickness = 350	500 * 500	600 * 400
8–10	500 * 500	600 * 400	Thickness = 250	400 * 400	600 * 400

strength of rebar is 400 MPa. Concrete slabs are at story levels with 150 mm thickness. In the analysis and design processes, all lateral displacement limitations and strength requirements, as mandated, have been checked in reference with UBC-97 [28] and ACI 318-11 [29]. The details along with the cross-sectional dimensions of the elements are presented in Table 1.

### 3. Description of Analytical Models

**3.1. Material Properties and Elements Type.** The analytical model behavior of the building is approximated by a continuous 3D finite element model using the OpenSees [27] nonlinear analysis program, as shown in Figure 2. Incremental dynamic time history analysis was conducted to determine the performance of the prototype buildings. To develop the analytical model inelastic force-based formulations were used for the simulation of nonlinear beam and column elements. Beam-column elements were modeled as fiber sections with distributed material plasticity along the element length. Geometric transformation to account for the *P-Delta* effect was used in the OpenSees model. *Concrete01* was used for simulating uniaxial Kent–Scott–Park concrete material behavior taking into account unloading and reloading stiffness based on the work of Karsan and Jirsa [30], with zero tensile strength. The reinforcing bars were modeled using the uniaxial *Steel01* to create a uniaxial bilinear steel material based on kinematic hardening defined by a nonlinear evolution equation.

**3.2. Modeling of Base Isolation System.** The analytical model of the lead rubber bearing (LRB) was generated using the elastomeric bearing element, which has a bilinear force-deformation response envelope as implemented in the OpenSees program. This isolation system consists of layers of thin steel shim and rubber, to provide vertical stiffness and horizontal flexibility. For dissipating the seismic energy and reducing the bearing displacement, a lead core has been inserted into the holes in the elastomeric bearing [31, 32]. Sixteen equally sized LRBs were considered to be located under the inner core columns between the foundation and beam-slab system, consisting of an orthogonal mesh of RC beams (650/650 mm) [33, 34]. The slabs at the base were identical to those of the other floors, as illustrated in Detail-1 of Figure 1. For dynamic analysis, the mass of the structure was lumped at the beam-column joint at each floor level. A rigid diaphragm was considered at each floor level in order to obtain the same lateral displacement across the floor. Applying rigid diaphragm constraints in the OpenSees models also reduced modeling complexity and analysis time [35, 36]. The design of superstructure

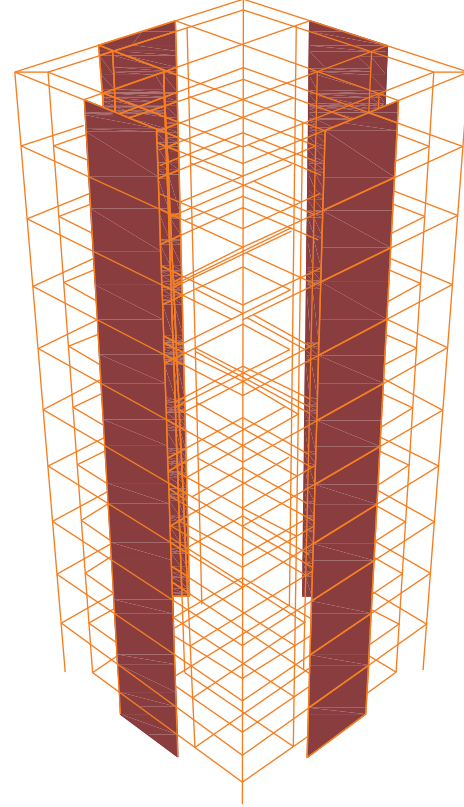


FIGURE 2: Three-dimensional (3D) analytical model of the prototype buildings.

is based on the design basis earthquake (DBE), while isolation devices should be designed for displacement obtained from maximum considered earthquake (MCE) [37]. The mechanical properties of the isolators were set to comply with the recommendation of the UBC building code subjected to critical reaction force in inner core columns. Moreover, the first mechanical characteristics of the isolators can be identified by the manufacturer [38], and the preyield stiffness ( $K_1$ ) can be either evaluated from available hysteresis loops obtained from elastomeric bearing tests or assigned as a factor of postyield stiffness ( $K_2$ ) [39]. Three parameters were used to simulate the nonlinear force-deformation behavior of the isolators through the bilinear hysteresis loop as shown in Figure 3 (b), namely, (i) preyield stiffness ( $K_1$ ) and (ii) postyield stiffness ( $K_2$ ), and characteristic strength ( $Q$ ).  $K_1$  is taken to be 10 times  $K_2$  [39–41].  $K_2$  and  $Q$  were initially calculated using estimated deformation of the bearings and the effective period of the building. The characteristic strength  $Q$  is estimated from the hysteresis loop for the elastomeric bearings, and for LRB systems,  $Q$  is given by

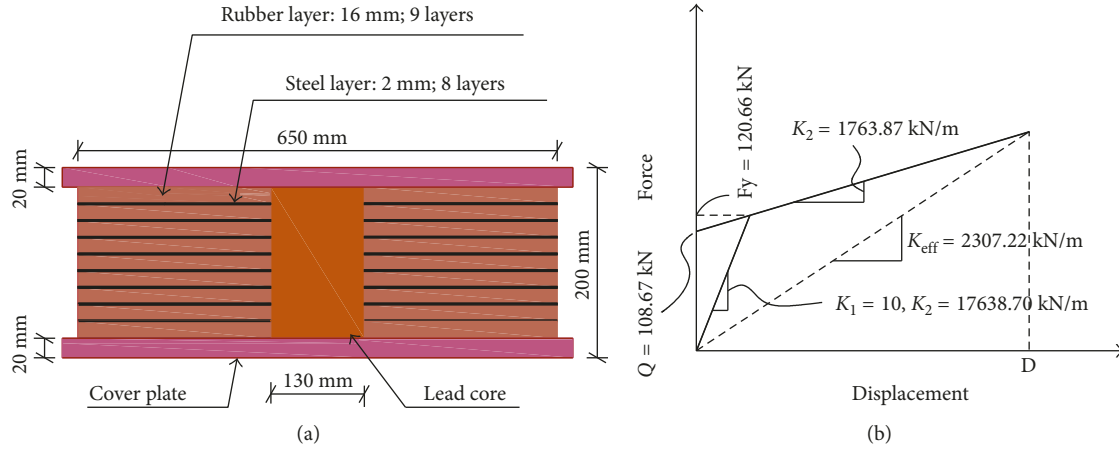


FIGURE 3: Details of the base isolation system: (a) cross-sectional configuration and (b) bilinear hysteretic model.

$$Q = A_{pb} \cdot \sigma_y, \quad (1)$$

where  $A_{pb}$  and  $\sigma_y$  are the area and yield stress of the lead, respectively, and  $\sigma_y$  is assumed to be 10 MPa. The total effective stiffness ( $K_{eff}$ ) of the isolation system is generally estimated by the fundamental isolation period of the building ( $T^{iso}$ ). In the case of isolated structures, base isolation is most appropriate when the isolation period was selected to be in the range between 1.5 and 3.0 s [42–44], which in this study was considered to be 2.0 s. The effective stiffness is expressed as

$$K_{eff} = m \times \left( \frac{2\pi}{T^{iso}} \right)^2, \quad (2)$$

where  $m$  is the total mass of the building, while the postyield stiffness  $K_2$  is given by the following formula:

$$K_2 = K_{eff} - \frac{Q}{D}, \quad (3)$$

where  $D$  is the design displacement. The compression stiffness of the bearing is determined by the axial stiffness and is given by the following formula:

$$K_V = \frac{E_c A}{t_r}, \quad (4)$$

where  $A$  is the cross-sectional area of the bearing;  $t_r$ , the total thickness of the rubber, is given by  $t_r = D/\gamma_{max}$  and taken as  $t_r = 160$  mm, where  $\gamma_{max}$  is maximum shear strain taken as 1.5, for all LRBs;  $E_c$  is the compression modulus of the rubber-steel and is given by  $E_c = 6GS^2$ , where the shape factor  $S$  of the bearing is assumed to take the value of 10 [39]; and  $G$  is the shear modulus of the elastomeric bearing amounts to 0.80 MPa [39, 45]. The properties used in the design LRB bearings are presented in Figure 3. For this study, the effective damping of an isolator  $\beta_{eff}$  is assumed to be equal to 15%. The compression stiffness of the bearing was determined as axial stiffness  $K_V$  and was set to 1301463.65 kN/m.

Base isolation requires a gap between the inner core and its surroundings to afford enough distance for the displacement of isolators. This gap should be appropriately preserved and must remain free through the entire life of the

structure [46, 47]. The separation gap should be enough to allow the movement of isolation devices in the horizontal plane without colliding with its surroundings. In addition, special architectural details must be included to limit pounding during strong earthquakes. In order to evaluate the gap size, the total maximum displacement of the isolation system ( $D_{TM}$ ), should be considered with regard to both the maximum translational displacement ( $D_M$ ) and the torsional displacement. This relation is given by

$$D_{TM} = D_M \left[ 1 + y \frac{12e}{b^2 + d^2} \right], \quad (5)$$

$$D_M = \frac{g}{4\pi^2} \frac{C_{VM} T^{iso}}{B_M},$$

where  $b$  is the short dimension of the structure measured perpendicular to the long dimension of the building ( $d$ ) and  $y$  is measured in the direction normal to the seismic loading from the center of rigidity of the isolation system and a corner. And  $e$  is the eccentricity between the center of mass of the superstructure and the center of rigidity of the isolation system considering 5% accidental eccentricity,  $g$  is the gravitational acceleration,  $C_{VM} = 1.152$  is the seismic coefficient, and  $B_M$  is a numerical coefficient related to the effective damping of the isolation system which is taken as 1.35, corresponding to damping coefficient of  $\beta_{eff} = 15\%$  [28]. The analytical gap distance is shown in Detail-1 of Figure 1.

### 3.3. Modeling of Multilayer Shell Element for Shear Wall.

The RC shear walls were simulated using the multilayered shell element *ShellMITC4*, proposed by Dvorkin et al. [48] based on the theory of mixed interpolation of tensorial components (MITC) with four nodes, which was already provided in OpenSees. The multilayered shell element is based on the principles of composite material mechanics and has several layers, of different thicknesses, with different multidimensional concrete [49, 50] as shown in Figure 4. In this study, the section of solid shear walls was modeled with eight-layer shell elements, including the

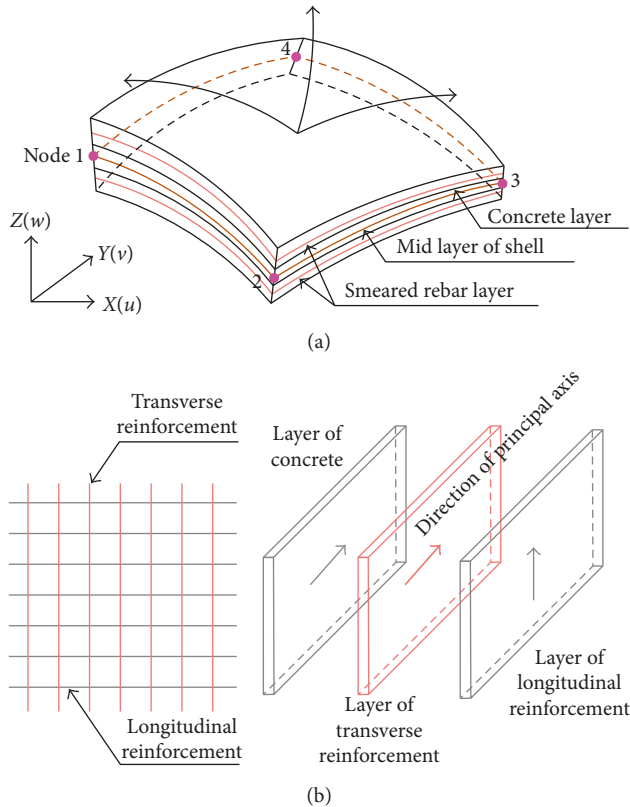


FIGURE 4: The principles of multilayer shell element for shear walls. (a) Multilayer shell element. (b) Distribution of the reinforcement layers.

multidimensional concrete, reinforcement material, with corresponding thicknesses.

#### 4. Ground Motion Ensemble

Nonlinear response history analysis was carried out on 3D OpenSees models of sample buildings. In the analytical models, 22 component pairs of horizontal ground motions were uniformly applied at the base of the buildings. Ground motion records selected were obtained from the next generation attenuation (NGA) project database developed by Pacific Earthquake Engineering Research (PEER) [51]. The records had a moment magnitude between 6.5 and 6.9, and the closest distance to fault rupture ranged from 13.9 to 37.7 km, all of which were recorded on stiff soil. For brevity, only the acceleration response spectrum (5% damped) for the selected set of ground motion records are presented in Figure 5. Characteristics of the selected records set are tabulated in Table 2 including the directional component ( $\phi$ ), which shows the direction of seismic input in  $E$  and  $N$  directions, where the letters  $E$  and  $N$  indicate the global direction of structures in  $X$  and  $Y$  directions, respectively, as illustrated in Figure 1(a), moment magnitude ( $M$ ), closest distance to fault rupture ( $R$ ), and peak ground acceleration (PGA) values. Ground motions are scaled to represent a range of earthquake intensities up to collapse level ground motions.

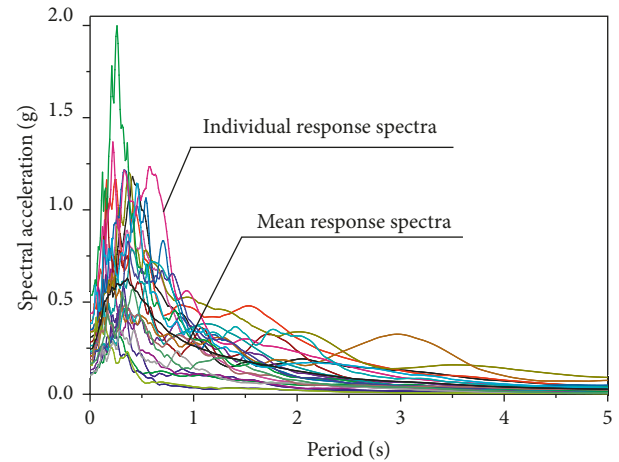


FIGURE 5: Acceleration response spectrum with 5% damping ratio for 22 ground motion records.

The selected ground motions in this study were scaled using the first-mode vibration period with 5% critical damping  $S_a(T_1, 5\%)$ , with each ground motion scaled such that the scale factor is used to match the spectral acceleration at the first-mode period of each structure to the design spectral acceleration [37]. Once the scaled records were generated, each record was incrementally scaled in multiple levels by an increment of 0.05 g in spectral acceleration to cover the entire range of structural response, from yielding zone to dynamic instability.

A value of 5% Rayleigh damping, mass, and stiffness proportional damping, was used in the dynamic analysis [52, 53]. The gravity load combinations for nonlinear analysis were different from design gravity load combinations, and effective seismic weight for each floor was estimated using the load combination  $1.05 \text{ DL} + 0.25 \text{ LL}$  [54, 55] and was converted to lumped masses at beam-column joint in the story levels for dynamic analysis, where DL is the nominal and superimposed dead load of the structure, and LL is the nominal live load.

#### 5. Incremental Dynamic Analysis (IDA)

IDA is a parametric analysis technique that has been recently developed to carefully estimate the seismic performance of structures using various nonlinear dynamic analyses under several scaled ground motion records. The method has been described in detail by Vamvatsikos and Cornell [56]. IDA requires conducting a series of nonlinear dynamic time history analyses for each record for producing one or more curves of engineering demand parameter (EDP) as a damage measure (DM) versus intensity measure (IM) curve under the effect of several scaled ground motions. The ground motions are characterized by the intensity measure (IM), which can be expressed in terms of peak ground acceleration (PGA), peak ground velocity (PGV), or spectral acceleration ( $S_a$ ). Damage measure (DM) can be defined and related to performance limit states of the structure corresponding to various damage levels. For the present study, spectral acceleration at the first-mode period of vibration with 5%

TABLE 2: Properties of twenty-two ground motion records used.

Number	Event	Year	Station	$M$	$R$ (km)	$\phi$	PGA (g)
1	Cape Mendocino	1992	Fortuna fire	7.01	20.41	E	0.283
						N	0.333
2	Cape Mendocino	1992	Centerville beach	7.01	18.31	E	0.318
						N	0.477
3	Duzce, Turkey	1999	Lamont	7.14	11.46	E	0.131
						N	0.101
4	Friuli Italy-01	1976	Tolmezzo	6.5	15.82	E	0.357
						N	0.315
5	Imperial Valley-06	1979	Calipatria fire	6.53	24.60	E	0.128
						N	0.078
6	Imperial Valley-06	1979	Superstition mtn.	6.53	24.61	E	0.111
						N	0.202
7	Irpinia Italy-01	1980	Calitri	6.9	17.64	E	0.126
						N	0.136
8	Irpinia Italy-01	1980	Brienza	6.9	22.56	E	0.219
						N	0.183
9	Kobe Japan	1995	Kakogawa	6.9	22.5	E	0.24
						N	0.324
10	Kocaeli Turkey	1999	Duzce	7.51	15.37	E	0.312
						N	0.364
11	Landers	1992	Coolwater	7.28	19.74	E	0.284
						N	0.417
12	Loma Prieta	1989	Gilroy-historic bldg.	6.93	10.97	E	0.242
						N	0.285
13	Loma Prieta	1989	Sunnyvale-colton ave.	6.93	24.23	E	0.2072
						N	0.2073
14	Northridge-01	1994	Beverly hills	6.69	18.36	E	0.621
						N	0.45
15	Northridge-01	1994	Canyon country	6.69	12.44	E	0.404
						N	0.472
16	Chuetsu-oki	2007	Kubikiku Hyakken	6.8	22.18	N	0.253
						E	0.214
17	Chuetsu-oki	2007	Shiura Nagaoka	6.8	20.17	N	0.22
						E	0.23
18	San Fernando	1971	Lake Hughes#9	6.61	22.57	E	0.170
						N	0.143
19	San Fernando	1971	Pasadena-CIT Athenaeum	6.61	25.47	E	0.097
						N	0.110
20	Spitak Armenia	1988	Gukasian	6.77	23.99	E	0.200
						N	0.174
21	Superstition Hills-02	1987	Plaster city	6.54	22.5	E	0.136
						N	0.200
22	Superstition Hills-02	1987	Poe road	6.54	11.6	E	0.475
						N	0.286

damping  $S_a(T_1, 5\%)$  was used as the seismic intensity measure (IM), and the maximum interstory drift ratio  $\theta_{\max}$  was considered as damage measure (DM). Maximum interstory drift ratio is defined as the difference between the maximum displacements of floors in a story, divided by the story height (e.g., maximum, overall stories, and peak interstory drift ratio  $\theta_{\max}$ ).

In order to consider the limiting values of damage levels for the derivation of seismic fragility curves, limit states should be described on the IDA curves. Some studies considered different damage levels. For example, three limit states have been suggested in FEMA 350 [57], such as immediate occupancy (IO), collapse prevention (CP), and global dynamic instability collapse. The first limit state (IO)

is defined at maximum interstory drift ratio  $\theta_{\max} = 2\%$ , whereas the collapse prevention (CP) is named on the median IDA curve using the 20% tangent slope scale. Finally, global dynamic instability occurs by increasing levels of IM at constant steps, when the *flatline* on the IDA curve is reached.

Dumova-Javanoska [58] and Altay et al. [59] defined different limit states, such as slight, moderate, extensive, and collapse as stated in HAZUS-MH [60], whereas Kirçil and Polat [61] specified two different damage levels, that is, yield point at the end of the linear path and collapse which occurs in the nonconverging run. In this study, yielding and collapse were considered as essential damage levels for which yield and collapse points are displayed in Figure 6(f).

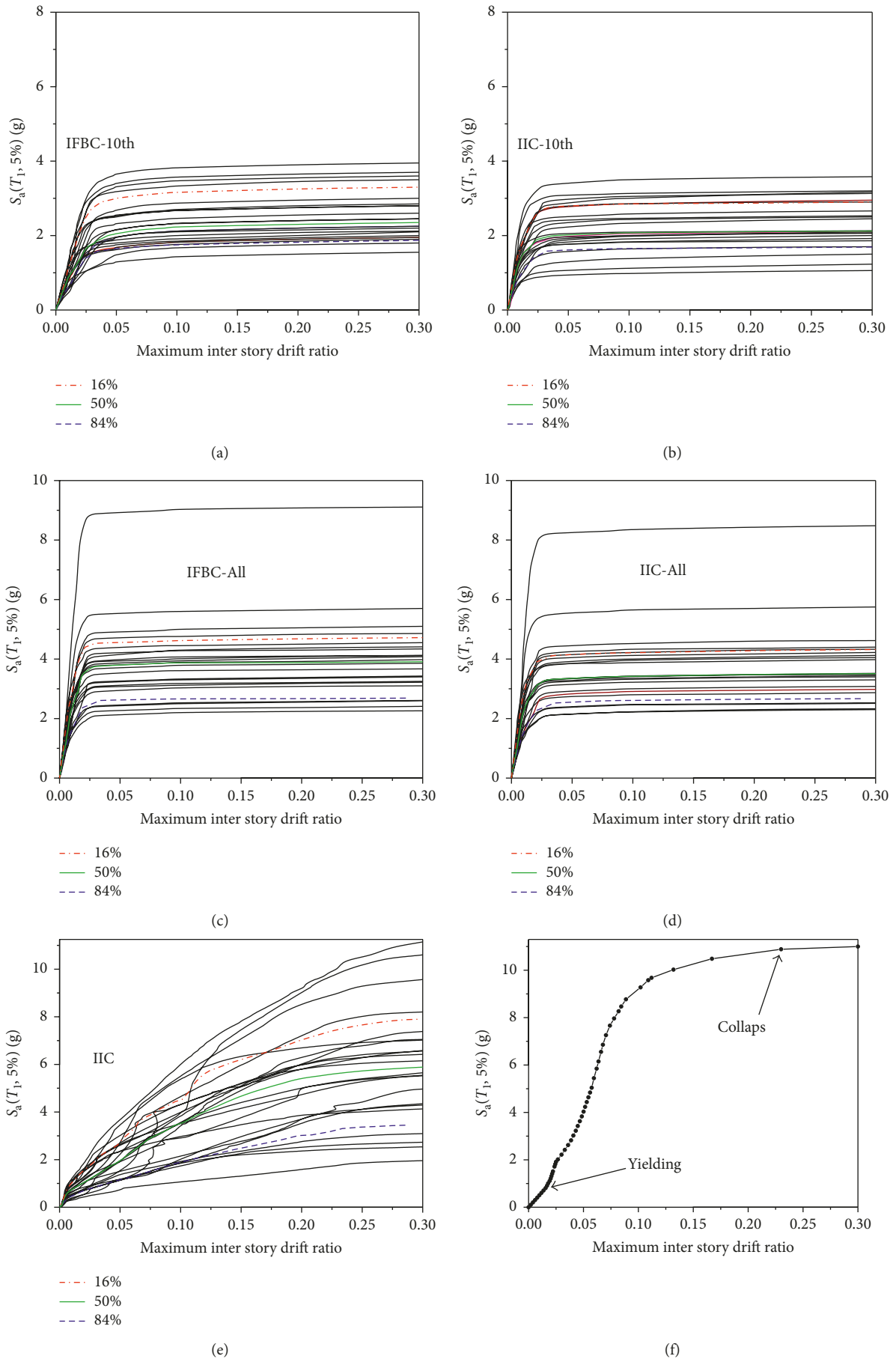


FIGURE 6: Continued.

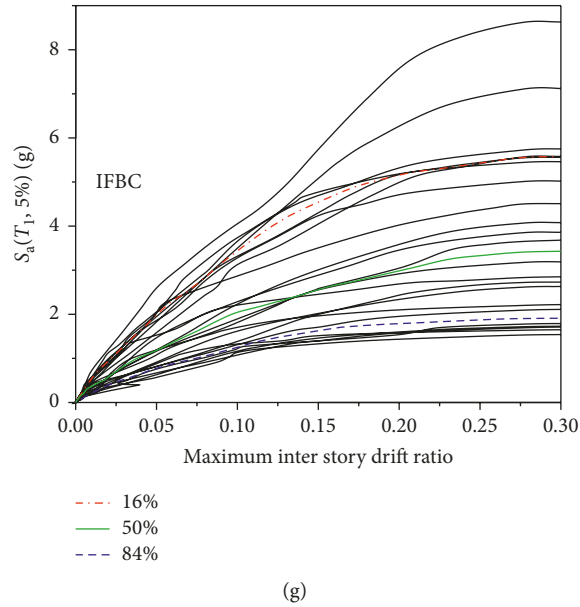


FIGURE 6: IDA curves of analysis models: (a) IFBC-10th, (b) IIC-10th, (c) IFBC-All, (d) IIC-All, (e) IIC, (f) single IDA curve to display yielding and collapse position, and (g) IFBC.

The yield structural capacity is defined by the point where the IDA curve starts to decline from the linear path, (i.e., the relationship between the maximum interstory drift ratio and spectral acceleration at the yield point of IDA curve is linear). Moreover, elastic IDA region can be defined as the region where the initial stiffness remains constant with increase in spectral acceleration with related slope remaining constant until a specific point (yield point) is reached. This is important since both slope and stiffness start changing with the increasing spectral acceleration. This attests to the elastic behavior of the structure. To identify the collapse capacity of structure, the selected earthquake records first need to be scaled with low values of IM and gradually increased to several higher IM levels until structural collapse occurs as a result of a numerical nonconverging run. In this study, the state of collapse capacity of the structure at the nonconverging run was considered as the limit state for failure.

The seismic performance of the six prototype buildings under IDA analysis was compared in terms of various performance criteria. Moreover, results from the IDA analysis were plotted as IDA curves in the IM-DM plane. In each plot, locating the maximum drift observed in an analysis gives one point in the IM versus DM ( $S_a$  versus  $\theta_{max}$ ) domain, and with increasing the values of IM, other points on each IDA curve are generated. Thus, IDA curves for six analytical models in the X-X direction are shown in Figure 6. Therefore, IDA curves exhibit an extensive range of structural behavior and large record-to-record variability. In such case, it is essential to summarize such dataset and quantify the randomness.

The results from IDA curves in the limit-state capacities (yielding and collapse) are tabulated in Tables 3–8 and also can be easily summarized into 16%, 50%, and 84% fractile values of DM and IM capacity for each limit state [62]. Summarized IDA curves were developed to estimate the

TABLE 3: Properties of yielding and collapse for IFBC-10th with respect to each record.

Number	$S_a(T_1, 5\%)$ (g)		$\theta_{max}$	
	Yielding	Collapse	Yielding	Collapse
1	0.847	3.105	0.00682	0.0266
2	0.26	1.196	0.00355	0.0373
3	0.378	1.344	0.00349	0.0193
4	0.252	1.638	0.00377	0.0293
5	0.6292	1.404	0.00643	0.0216
6	0.3855	2.1074	0.00387	0.0241
7	0.249	1.6185	0.00316	0.032
8	0.2512	2.01	0.00308	0.0287
9	0.911	2.125	0.00704	0.0223
10	0.40	2.00	0.00408	0.0343
11	0.2792	2.513	0.00388	0.0194
12	0.2296	1.435	0.00303	0.0466
13	0.720	1.620	0.00877	0.0201
14	0.1161	1.4706	0.00137	0.0232
15	0.660	2.860	0.00522	0.0276
16	0.4432	1.2742	0.00526	0.0181
17	0.9204	2.9146	0.00906	0.0298
18	0.5346	2.3166	0.00595	0.0293
19	0.1344	1.68	0.00239	0.0264
20	0.3376	1.7724	0.00556	0.0309
21	0.1779	1.6604	0.00229	0.0261
22	0.5577	2.2308	0.00566	0.0232

variation of structural capacities as shown in Table 9. Figures 6(c), 6(d), and Table 9 show approximately similar performance for structures IFBC-All and IIC-All for all the 16%, 50%, and 84% fractile IDA curves. The structural capacities of all prototype buildings at the collapse damage level were estimated through IDA on the median (50%) percentile, which defines the capacity of structures as the last IDA point in the nonconverging run. The median collapse

TABLE 4: Properties of yielding and collapse for IIC-10th with respect to each record.

Number	$S_a(T_1, 5\%)$ (g)		$\theta_{max}$	
	Yielding	Collapse	Yielding	Collapse
1	0.1482	2.2971	0.00136	0.0115
2	0.104	0.78	0.00146	0.0134
3	0.056	0.70	0.000863	0.00868
4	0.0471	2.0253	0.000617	0.0199
5	0.088	1.232	0.000962	0.0128
6	0.1656	3.0636	0.00149	0.030
7	0.1188	2.0196	0.00135	0.0251
8	0.1252	2.2849	0.00162	0.0185
9	0.0994	1.1928	0.00116	0.0142
10	0.0795	1.51	0.00105	0.027
11	0.074	1.998	0.00106	0.00848
12	0.1066	1.1193	0.00169	0.0211
13	0.093	1.395	0.000965	0.0128
14	0.0885	1.475	0.00176	0.0127
15	0.0821	2.7914	0.000787	0.0279
16	0.0982	1.1779	0.0012	0.00824
17	0.1384	2.2144	0.00152	0.0215
18	0.1408	1.6896	0.00155	0.0112
19	0.0666	2.0646	0.00148	0.0157
20	0.0944	2.4518	0.00138	0.0214
21	0.126	1.512	0.0014	0.0182
22	0.1242	1.1592	0.00166	0.00712

TABLE 5: Properties of yielding and collapse for IFBC-All with respect to each record.

Number	$S_a(T_1, 5\%)$ (g)		$\theta_{max}$	
	Yielding	Collapse	Yielding	Collapse
1	0.424	8.056	0.00152	0.0175
2	1.302	3.162	0.0044	0.0142
3	0.255	2.295	0.000759	0.00627
4	0.1966	2.8507	0.000682	0.00823
5	0.0456	1.5504	0.000211	0.00988
6	0.1281	2.135	0.000688	0.00863
7	0.429	3.6834	0.00113	0.0195
8	0.2536	2.7262	0.000871	0.00951
9	0.1017	3.9667	0.000433	0.015
10	0.9252	3.701	0.00417	0.02
11	0.13	3.77	0.000509	0.00141
12	0.2064	2.476	0.000859	0.0113
13	0.269	3.104	0.00137	0.0228
14	0.3682	2.2618	0.00145	0.0116
15	0.2358	3.4191	0.00173	0.0183
16	0.3416	1.7934	0.00117	0.00794
17	0.141	3.525	0.000604	0.0183
18	0.066	1.694	0.00032	0.0112
19	0.072	1.728	0.000377	0.0127
20	0.2673	2.0493	0.00129	0.0157
21	0.3504	2.7156	0.00165	0.0115
22	0.393	4.32	0.00117	0.0128

and yielding capacities for models IFBC-All and IIC-All are 2.788, 2.684 and 0.254, 0.264 with corresponding maximum interstory drift ratio ( $\theta_{max}$ ) of 0.01275, 0.0115 and 0.001, 0.00115, respectively, with a minor difference of 0.104 in terms of  $S_a$ , which means that the SBI with inner isolated

TABLE 6: Properties of yielding and collapse for IIC-All with respect to each record.

Number	$S_a(T_1, 5\%)$ (g)		$\theta_{max}$	
	Yielding	Collapse	Yielding	Collapse
1	0.296	6.9069	0.0011	0.0153
2	1.023	3.348	0.00349	0.0161
3	0.546	2.886	0.00172	0.00874
4	0.306	4.284	0.000936	0.0115
5	0.3616	1.4012	0.002	0.00919
6	0.0826	1.6107	0.000451	0.00724
7	0.20	2.0028	0.000527	0.00767
8	0.142	2.76	0.000376	0.0104
9	0.294	2.937	0.00151	0.016
10	0.6384	3.5112	0.00284	0.0181
11	0.514	3.4695	0.00181	0.0138
12	0.2943	2.7468	0.00128	0.0157
13	0.882	2.45	0.00439	0.0181
14	0.271	1.2792	0.00114	0.00641
15	0.121	2.057	0.000896	0.00857
16	0.2511	2.4273	0.000877	0.0116
17	0.1432	2.5776	0.000649	0.0142
18	0.0516	1.47	0.000261	0.0112
19	0.177	1.54	0.0011	0.0115
20	0.2046	2.622	0.001	0.0229
21	0.258	2.752	0.00127	0.0117
22	0.10	2.9	0.000346	0.00974

TABLE 7: Properties of yielding and collapse for IIC with respect to each record.

Number	$S_a(T_1, 5\%)$ (g)		$\theta_{max}$	
	Yielding	Collapse	Yielding	Collapse
1	0.0955	1.8145	0.00327	0.238
2	0.08	7.68	0.00188	0.212
3	0.078	5.616	0.00164	0.178
4	0.0699	5.7551	0.0018	0.185
5	0.0849	2.0942	0.00187	0.131
6	0.0671	2.7648	0.00182	0.201
7	0.087	9.483	0.00177	0.215
8	0.092	6.003	0.00218	0.182
9	0.072	6.912	0.00161	0.246
10	0.038	1.634	0.002	0.0823
11	0.081	3.861	0.00191	0.2
12	0.0762	8.3058	0.00181	0.19
13	0.0685	5.1375	0.00164	0.30
14	0.095	5.852	0.00232	0.188
15	0.087	3.654	0.00224	0.208
16	0.061	3.599	0.00145	0.106
17	0.07	4.97	0.0015	0.20
18	0.053	6.3648	0.00132	0.138
19	0.068	5.18	0.00155	0.161
20	0.0726	5.232	0.00158	0.245
21	0.053	10.335	0.00132	0.237
22	0.052	3.718	0.00149	0.201

core, as connected to the outer frames at all floor levels, has somewhat similar performance compared to that of IFBC-All. In addition, based on an eigenvalue analysis as stated in Section 7, the time period of both IFBC-All ( $T = 0.3947$  s) and IIC-All ( $T = 0.40$  s) also has a minor difference in the

TABLE 8: Properties of yielding and collapse for IFBC with respect to each record.

Number	$S_a(T_1, 5\%)$ (g)		$\theta_{max}$	
	Yielding	Collapse	Yielding	Collapse
1	0.01044	1.661	0.00232	0.2308
2	0.1546	3.588	0.00396	0.2563
3	0.1210	1.992	0.00268	0.2171
4	0.105	1.607	0.00282	0.2148
5	0.0887	1.447	0.00197	0.2065
6	0.140	1.694	0.00374	0.2247
7	0.2116	5.424	0.00363	0.2119
8	0.100	5.243	0.00220	0.2108
9	0.1456	5.326	0.00276	0.2367
10	0.0534	2.152	0.00199	0.2374
11	0.0895	2.650	0.00179	0.2447
12	0.0892	4.763	0.00176	0.2090
13	0.0882	2.585	0.00175	0.2657
14	0.1031	7.039	0.00119	0.2679
15	0.0895	1.508	0.00204	0.1479
16	0.1085	4.257	0.00219	0.2327
17	0.1736	3.970	0.00407	0.2567
18	0.0683	2.618	0.00148	0.1836
19	0.1110	5.130	0.00214	0.1963
20	0.1004	3.097	0.00203	0.2439
21	0.1438	8.181	0.00298	0.2311
22	0.0651	3.574	0.00121	0.2211

first-mode vibration period. It can be explained by the fact that the behavior of the structures cannot be significantly changed by using the base isolation devices in the inner columns in the cases where the inner structure is connected to the outer fixed base frames at all floor levels (e.g., IIC-All).

Using the base isolation system in the structures with long time period cannot be significantly effective. Whereas, as illustrated in Table 9, results from analysis of the isolated structure (e.g., IIC) embedded into the outer stiff frames with fixed bases while connected to the outer frames only at the topmost floor (e.g., IIC-10th) show that time period and interstory drift ratio decrease from 0.87 s to 0.569 s and 0.20 to 0.0149, respectively, even in comparison to the IFBC-10th structure. Comparing the elastic behavior of the SBI structure, Figures 6(b) and 6(e) show that IIC-10th and IIC have a similar elastic behavior with a short elastic region and both reach yielding capacity quite early. From Table 9, we can see that in terms of collapse capacity, the IFBC model when compared to those with embedded outer stiff frames (e.g., IFBC-All) displayed a marked reduction of 16.42% and 94.40% in spectral acceleration and interstory drift ratio, respectively.

## 6. Fragility Analysis Procedure

Once the IDA is completed, fragility curves can be obtained. Based on the results of the distribution of nonlinear dynamic analysis, fragility curves can be employed to quantitatively estimate the collapse capacity of the structures. A fragility curve relies on a graphical relationship of the probability of exceeding specific damage levels in terms of yielding and

collapse due to earthquake as a function of given intensity. It is generally expressed in the form of two-parameter lognormal distribution function. Based on this statement, the cumulative probability of exceeding damage levels modified on the IM is expressed as

$$P[D|M] = \phi\left(\frac{\ln(IM) - \lambda}{\sigma}\right), \quad (6)$$

where  $\phi$  is the standard normal distribution, IM is the intensity measure of the earthquake in term of  $S_a$ ,  $D$  is the damage level, and  $\lambda$  and  $\sigma$  are the mean and standard deviation of  $\ln(IM)$ . The mean and standard deviation of  $\ln(IM)$  values corresponding to the prescribed limit states are determined based on a regression analysis of the IDA results for each structural model [63]. Table 10 summarizes the mean and standard deviation of lognormal distributed intensity measure in terms of  $S_a$  for each damage level obtained using the median collapse intensity and lognormal distributed ground motion ( $S_a$ ).

The fragility curves of the model structures constructed for yielding and collapse together are depicted in Figure 7. From the yield probability curves in Figure 7(a), it can be observed that the movement of yielding curves from right to left could be attributed to the reduction in yielding capacity of structures. Generally, flatter curves (e.g., IFBC-10th, IFBC-All, and IIC-All) exhibit a longer elastic range, whereas when the slope of the yielding curves continually increase (e.g., IIC-10th, IIC, and IFBC), elastic range becomes short and maximum yielding capacity is reached early. As one would expect, the yielding phenomenon is generally higher when the inner core is completely connected to the outer frame in more floor levels. This means that the elastic range in model IIC-10th can be changed from higher to lower values by connecting the inner core in some floor to the outer frames. As mentioned earlier, Figures 6(b) and 6(e) indicate that the elastic behavior of IIC-10th and IIC are very close to each other.

Figure 7(b) depicts the collapse probability of sample buildings in terms of  $S_a$ . From this figure, it is evident that the IIC structure has significantly lower collapse probability compared to that of IFBC-10th, IIC-10th, IFBC-All, IFBC, or IIC-All. Moreover, fragility curves for IFBC-All and IIC-All indicate that when the inner isolated core is connected to the outer frame at all floor levels, the behavior of the structure is very close to that of IFBC-All structure. Moreover, Figure 7(b) shows that collapse probability of IIC-10th is higher, and it continues to decrease with the increase in the IM. This pattern can be numerically simulated at any specified higher IM levels. For example, given the spectral acceleration in  $S_a = 3.0$  g (also indicated in Figure 7(b)), the corresponding collapse probability are 18.25%, 56.37%, 67.30%, 94.26%, 70.92%, and 41.58% for the IIC, IFBC-All, IIC-All, IFBC-10th, IIC-10th, and IFBC, respectively. From this analysis, it can be concluded that the IIC-10th structure has reduced collapse probability at higher IM ranges of approximately 25% when compared to that of IFBC-10th. Furthermore, Figure 7(b) shows that all prototype models, in contrast to model IIC-10th, have lower collapse probability. Moreover, models IFBC-All and IIC-All with all connected floors have

TABLE 9: 16%, 50%, and 84% fractile values in terms of DM and IM for yielding and collapse.

Structures	Limit state	16%		50%		84%	
		$S_a(T_1, 5\%)$ (g)	$\theta_{max}$	$S_a(T_1, 5\%)$ (g)	$\theta_{max}$	$S_a(T_1, 5\%)$ (g)	$\theta_{max}$
IFBC-10th	Yielding	0.2366	0.00304	0.382	0.00398	0.698	0.00668
	Collapse	1.415	0.0206	1.73	0.0265	2.44	0.0316
IIC-10th	Yielding	0.076	0.00096	0.099	0.00137	0.134	0.00159
	Collapse	1.166	0.0096	1.601	0.0149	2.293	0.0238
IFBC-All	Yielding	0.1112	0.00046	0.2543	0.0010	0.4128	0.0016
	Collapse	1.8855	0.008914	2.7884	0.01275	3.7451	0.0183
IIC-All	Yielding	0.12856	0.000478	0.2645	0.0011	0.53448	0.00193
	Collapse	1.565	0.00863	2.684	0.01155	3.4257	0.01595
IIC	Yielding	0.0559	0.00149	0.0723	0.00178	0.087	0.00211
	Collapse	3.065	0.15204	5.206	0.20	7.403	0.2760
IFBC	Yielding	0.0884	0.00177	0.1037	0.00216	0.151	0.0034
	Collapse	1.673	0.207	3.336	0.2277	5.296	0.2521

TABLE 10: Properties of fragility curves parameters.

Structures	Yielding		Collapse	
	$\lambda$	$\sigma$	$\lambda$	$\sigma$
IFBC10th	0.983	0.598	0.619	0.271
IIC-10th	2.318	0.316	0.481	0.391
IFBC-All	1.471	0.809	1.037	0.384
IIC-All	1.383	0.748	0.921	0.396
IIC	2.643	0.227	1.555	0.504
IFBC	2.239	0.327	1.155	0.526

approximately identical performance pertaining to collapse phenomenon. Therefore, in double-skin SBI structures, the probability of collapse can be reduced by connecting more floor levels to the outer frames.

## 7. Seismic Responses of Prototype Buildings

An eigenvalue analysis was conducted to better understand the response of the prototype buildings. This analysis elicits the calculation of time periods and vibration modes of the structures. To validate the consistency of the analytical models, structural periods and vibration modes of sample models simulated in ETABS [39] and OpenSees were compared. Therefore, in this study, time period of first three modes and vibration modes built in OpenSees and ETABS were compared, as shown in Tables 11–13. Results from Tables 11–13 are compared in this section to have a better understanding and also to corroborate the capabilities of the SBI system. Table 13 shows the time period of first three modes for all prototype models. For brevity, only the first three modes of vibration for the model inner fixed base core (IFBC) is tabulated in Tables 11 and 12. Results indicate that the time period and vibration modes obtained from OpenSees program matched very well with those of ETABS software.

Table 13 indicates that the time period in double-skin SBI structure can be changed by increasing the number of connected floor levels. Except IIC-10th, all other kinds of double-skin structures (e.g., IFBC-All, IIC-All, IIC-10th, and IFBC-10th) have a lower time period. This indicates that as the number of connected floors increases,

the time period significantly decreases. Based on this statement, it can be also noted that when an isolated structure with long time period is encased and embedded inside a stiff outer frame to create a double-skin SBI structure, the time period needs to be limited to a reasonable range of 1.5–3.0 s [42–44], by using more coupling beams in any floor level. It means that the dynamic characteristics of SBI structure such as time period can be drastically adjustable.

To evaluate the effectiveness of LRB isolation system in the SBI building, nonlinear dynamic analyses were performed with selected ground motions mentioned above. The seismic responses of prototype buildings were compared in terms of maximum absolute roof acceleration, maximum absolute roof displacement, and maximum absolute base shear force. The resulting curves extracted from a single-record IDA study subjected to Northridge-01, 1994 (no. 14) ground motion data were compared for each model. The no. 14 ground motion possess 0.621 PGA with duration of 24 (s). Figures 8 and 9 show the predicted time history of the earthquake responses in the nonlinear time history analysis on six comparative models subjected to no. 14 ground motion. For better understanding, the maximum absolute responses such as accelerations, displacement, and base shear force are tabulated in Table 14.

As stated in previous sections, seismic behavior of model IFBC-All and that of model IIC-All are very close to each other. Furthermore, results from this section significantly corroborate the above statement. From Table 14, maximum absolute floor acceleration and displacement for the IFBC-All are 17.95 (g) and 0.128 (m), respectively, which is somewhat close to the IIC-All with maximum absolute floor acceleration and displacement of 17.80 (g) and 0.126 (m), respectively.

By comparing the model IIC with other five models, it is deduced that the maximum absolute roof displacement experienced in the IIC (0.19 m) is larger than the maximum absolute roof displacement in other five. Thus, embedding model IIC in the outer frames (as in IIC-10th and IIC-All), roof displacement is decreased by approximately 32%, while roof acceleration in model IIC (8.66 (g)) is drastically reduced.

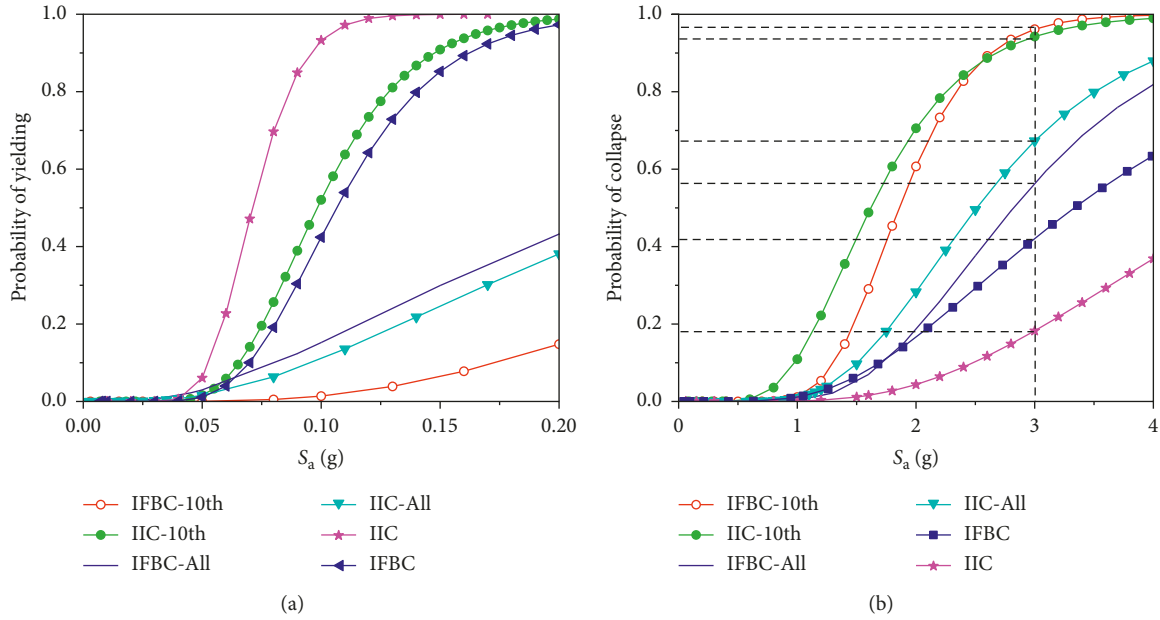


FIGURE 7: (a) Fragility curves for yielding and (b) fragility curves for collapse.

TABLE 11: Periods  $T_i$  and mode shapes  $\Phi_i$  for the first three modes of vibration based on OpenSees program for model IFBC.

$T_i$	$\Phi_i$	Number of story									
		1st	2nd	3rd	4th	5th	6th	7th	8th	9th	10th
$T_1 = 0.717$	$\Phi_1$	0.203	0.270	0.465	0.610	0.731	0.762	0.803	0.878	0.942	1.00
$T_2 = 0.715$	$\Phi_2$	-0.414	-0.553	-0.652	-0.587	-0.387	0.00	0.331	0.711	0.921	1.00
$T_3 = 0.653$	$\Phi_3$	0.768	0.997	0.689	-0.0605	-0.325	-0.602	-0.945	-0.812	0.0801	1.00

TABLE 12: Periods  $T_i$  and mode shapes  $\Phi_i$  for the first three modes of vibration based on ETABS program for model IFBC.

$T_i$	$\Phi_i$	Number of story									
		1st	2nd	3rd	4th	5th	6th	7th	8th	9th	10th
$T_1 = 0.783$	$\Phi_1$	0.161	0.292	0.434	0.555	0.696	0.808	0.787	0.929	0.969	1.00
$T_2 = 0.779$	$\Phi_2$	-0.388	-0.601	-0.744	-0.648	-0.399	0.00	0.373	0.636	0.858	1.00
$T_3 = 0.694$	$\Phi_3$	0.802	1.00	0.787	0.253	-0.456	-0.645	-0.991	-0.924	-0.167	1.00

TABLE 13: Fundamental period of prototype structures.

Structures	Opensees model	ETABS model
IFBC-10th	0.51	0.538
IIC-10th	0.569	0.624
IFBC-All	0.3947	0.446
IIC-All	0.4	0.432
IIC	0.87	0.909
IFBC	0.717	0.783

As can be seen from Table 14, the roof acceleration and roof displacement of model IIC-10th were (resp.) 0.70 and 0.72 times that of model IFBC-10th, which means that the base isolation devices can drastically reduce earthquake responses of building.

Figure 9 shows base shear-displacement hysteresis curves. The total base shear forces are estimated by summing the horizontal reaction of the force developed in the cross

section of column bases. The model IIC showed lower total base shear forces compared to those of the other four models. Figure 9(b) and Table 14 show that IIC-10th has slightly better performance in reducing the seismic responses of building in comparison to models IFBC-10th, IFBC-All, IIC-All, and IFBC.

In general, the purpose of base isolation systems is to minimize the damage of the structural and nonstructural elements due to ground shaking. As seen in this section, isolated structures (e.g., model IIC) has the largest roof displacement when compared with other prototype models, with large displacement causing damage in the structural elements. Therefore, using SBI systems in this study and encasing the isolated structures with stiff outer frames resulted in model IIC-10th showing substantially reduced displacement, while acceleration and base shear could not be reduced the increase in the stiffness of the structure caused by connecting the topmost floor to the outer frames, when

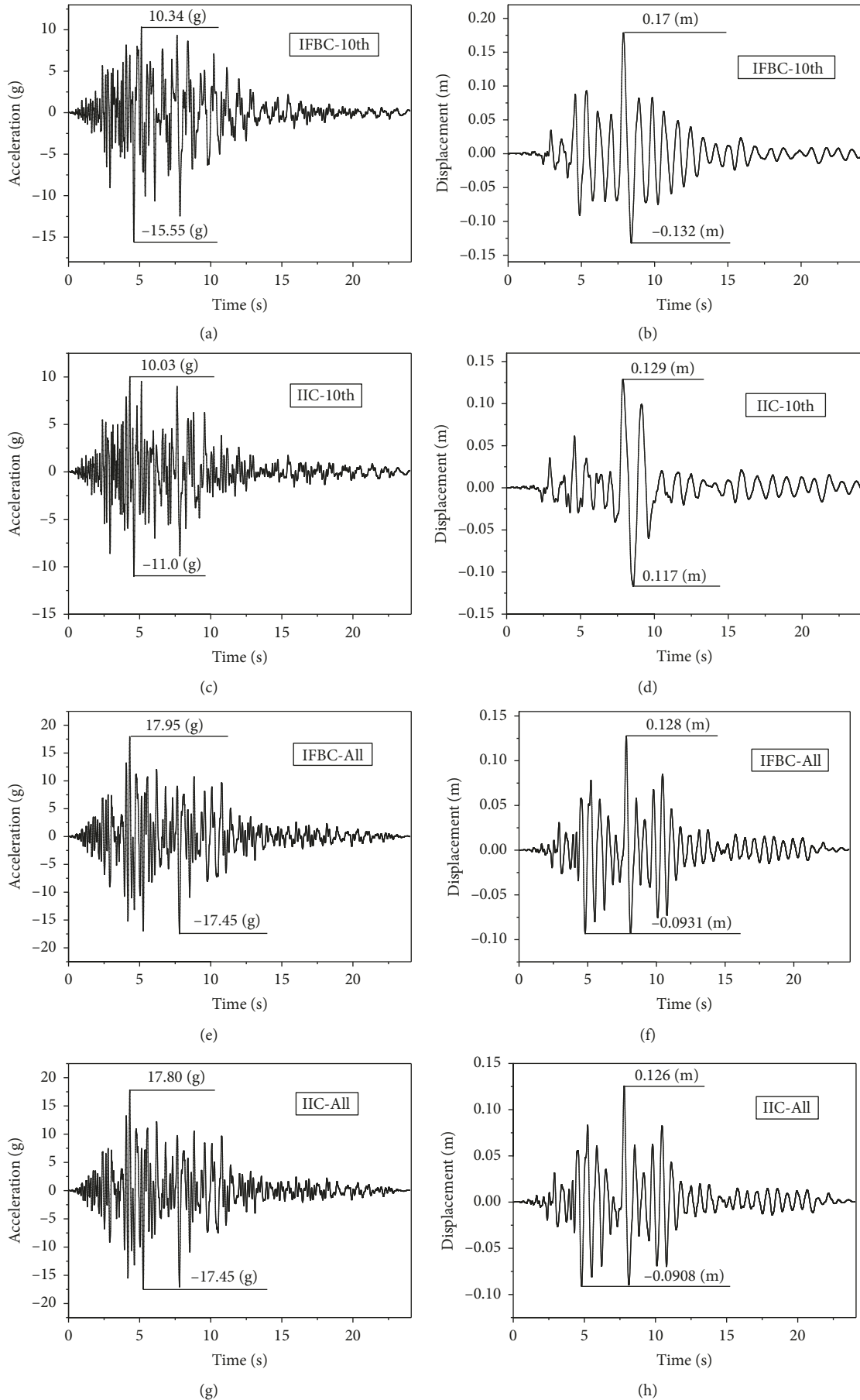


FIGURE 8: Continued.

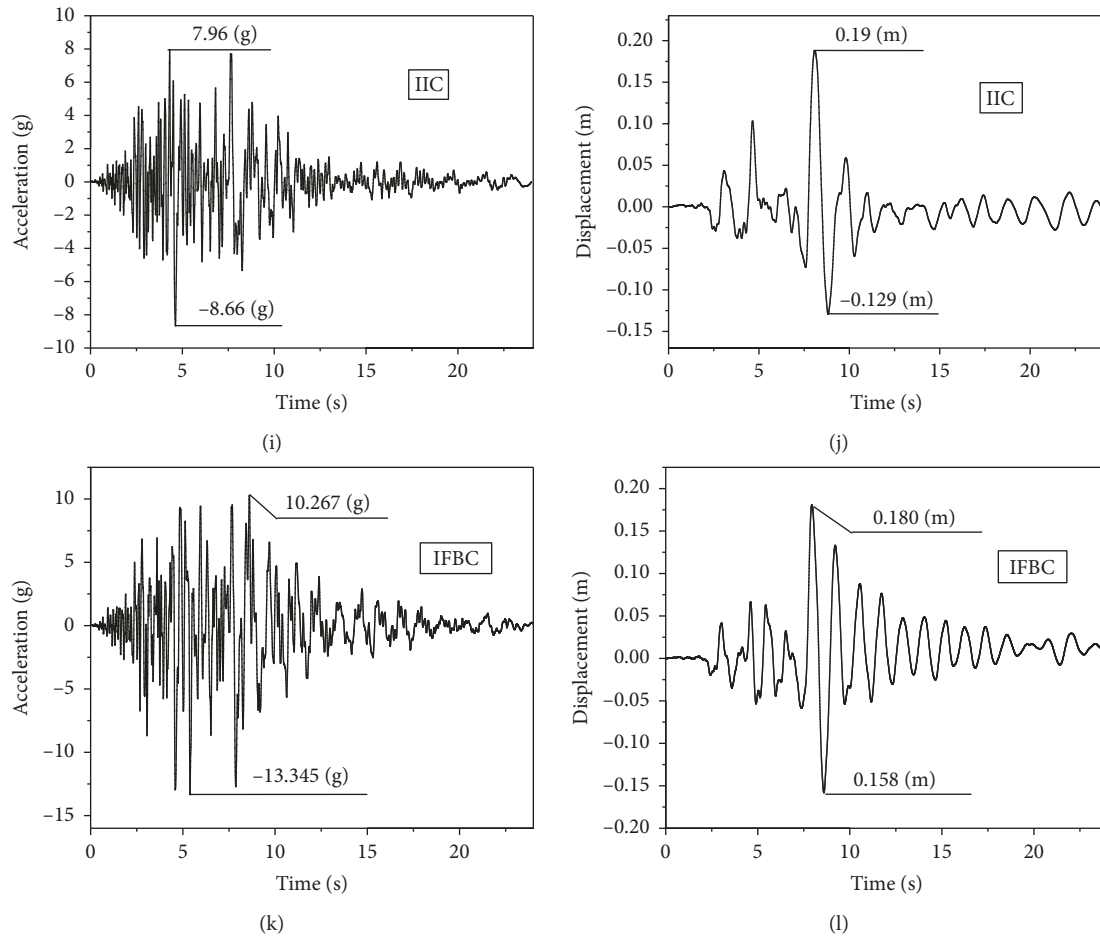


FIGURE 8: Time history of maximum absolute roof acceleration and roof displacement. (a) Time versus roof acceleration (IFBC-10th). (b) Time versus roof displacement (IFBC-10th). (c) Time versus roof acceleration (IIC-10th). (d) Time versus roof displacement (IIC-10th). (e) Time versus roof acceleration (IFBC-All). (f) Time versus roof displacement (IFBC-All). (g) Time versus roof acceleration (IIC-All). (h) Time versus roof displacement (IIC-All). (i) Time versus roof acceleration (IIC). (j) Time versus roof displacement (IIC). (k) Time versus roof acceleration (IFBC). (l) Time versus roof displacement (IFBC).

compared to that of the IIC model. However, SBI system and specifically model IIC-10th reduce both the acceleration and base shear in comparison to the IFBC-10th, IFBC-All, IIC-All, and IFBC with comparably similar displacements. It is clear that when using the coupling beams in more floor levels (e.g., IIC-All), the seismic behavior of SBI structures becomes closer to that of the structure with entire fixed base (e.g., IFBC-All). It means that the effectiveness of using the base isolation devices in double-skin SBI structure when all floor levels are connected to the outer frames is somewhat trivial.

It is therefore evident that in an SBI system, a model configuration between models IIC-All and IIC-10th, for example, with two connected floor levels, can be appropriate.

As mentioned earlier, due to the overturning action due to lateral forces, a tensile force (uplift) arises in the lateral force resisting system (LFRS). In some cases, the uplift due to the isolators located under the LFRS may cause instabilities in the isolation systems. To avoid this uplift force in the

isolation devices, double-skin SBI systems can have their entire LFRS removed from the inner isolated structure into the outer frames with fixed bases.

### 8. Conclusions

A numerical model has been presented for simulating the behavior of 3D 10-story double-skin SBI structure, using incremental dynamic analysis (IDA) subjected to 22 pairs of bidirectional scaled ground motion records. The results of the analysis of the sample structures were compared to those of the structures with added coupling beam at every floor level to investigate the seismic behavior of double-skin SBI buildings. Time-history analysis was also conducted using representative Northridge-01, 1994 (no. 14) ground motion data in terms of maximum absolute roof acceleration, maximum absolute roof displacement, and maximum absolute base shear force. Based on the results obtained from the IDA and fragility and time-history analysis, the following conclusions are drawn:

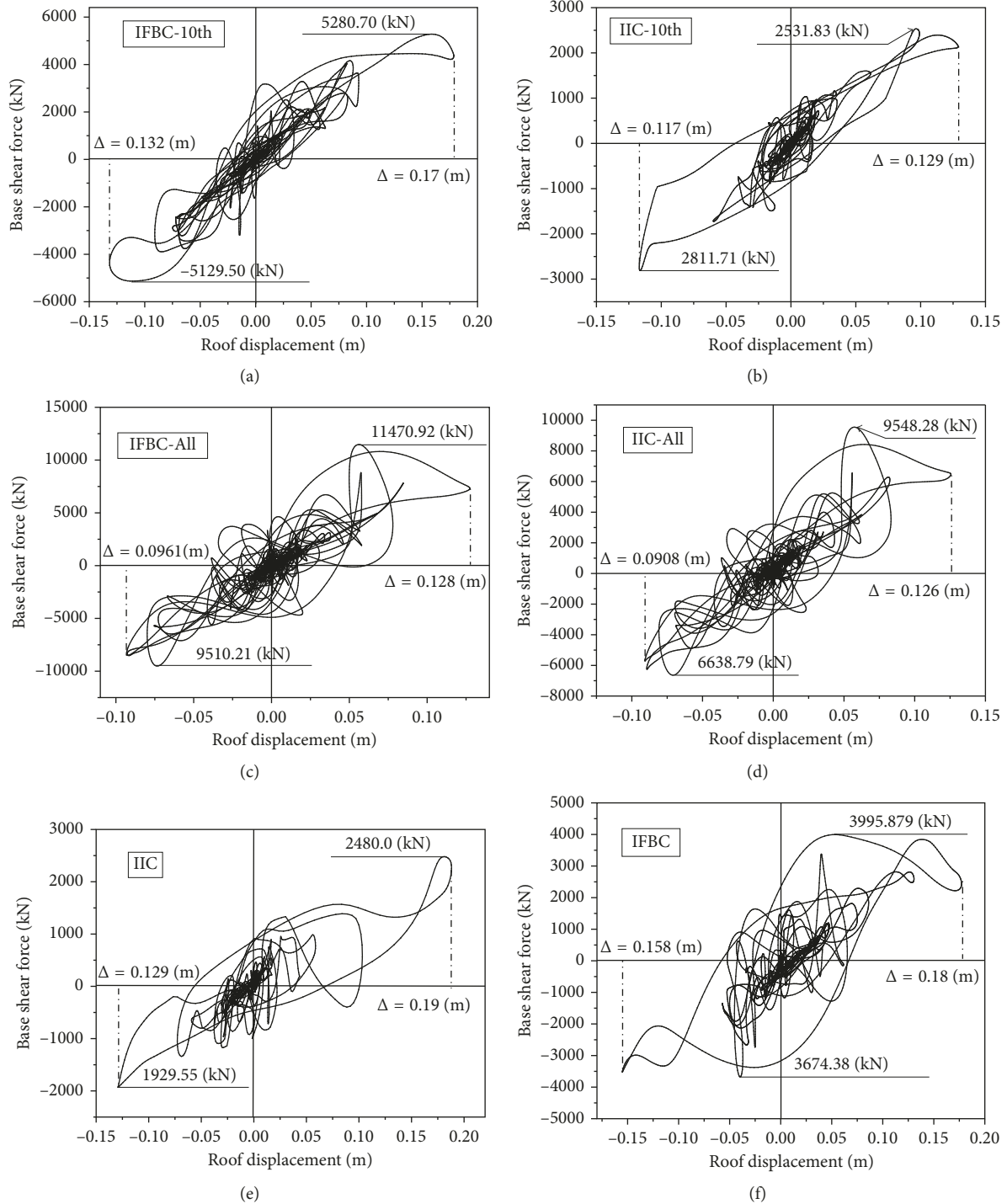


FIGURE 9: Base shear-roof displacement responses envelopes of prototype buildings. (a) Base shear versus roof displacement (IFBC-10th). (b) Base shear versus roof displacement (IIC-10th). (c) Base shear versus roof displacement (IFBC-All). (d) Base shear versus roof displacement (IIC-All). (e) Base shear versus roof displacement (IIC). (f) Base shear versus roof displacement (IFBC).

- (1) By comparing values from the elastic region obtained from the IDA, it was found that both the IIC-10th and IIC were subject to a lower elastic region and reached yielding capacity much earlier than that of IFBC-10th, IFBC-All, and IIC-All.
- (2) Results showed that for models with inner isolated core connected to the outer frames at all floor levels (model IIC-All), the earthquake responses of structures such as collapse and yielding capacity, interstory drift ratio  $\theta_{max}$ , and also spectral acceleration  $S_a$  are

TABLE 14: Maximum absolute roof acceleration, displacement, and base shear.

Structures	Acceleration (g)	Displacement (m)	Base shear (kN)
IFBC-10th	15.55	0.170	5280.70
IIC-10th	11.0	0.129	2811.71
IFBC-All	17.95	0.128	11470.92
IIC-All	17.80	0.126	9548.28
IIC	8.66	0.19	2480.0
IFBC	13.345	0.18	3995.879

very similar to the model with the inner fixed base core (model IFBC-All). This implies that the benefits of base isolation in SBI system are reduced if the inner isolated core is connected to the outer frames at all floor levels.

- (3) In contrast to IIC (with time period  $T = 0.87$  s and interstory drift ratio  $\theta_{\max} = 0.20$ ), IIC-10th (with  $T = 0.569$  s and  $\theta_{\max} = 0.0149$ ) has both shorter time period and reduced interstory drift ratio, it can thus be proposed that isolated structures that have long time period and large displacement when encased and embedded inside a stiff outer frame result in reduced responses. It means that double-skin SBI system can be significantly more effective than isolated structures with long time period and large lateral displacement.
- (4) Results from the collapse probability curves show that except model IIC-10th, all prototype models have approximately lower collapse level, and models IFBC-All and IIC-All with all floors connected with the outer frame have approximately identical performance in relation to collapse. It can be observed that for double-skin SBI system with increased number of connected floor levels, the probability of collapse decreases. Therefore, with respect to model IIC-10th, it is better to increase the number of connected floors, while with respect to model IIC-All it is better to decrease the number of connected floors.
- (5) Eigenvalue analysis shows that the time period in double-skin SBI structure can be changed by increasing the number of connected floors. Except IIC-10th, all other kinds of double-skin structures (e.g., IFBC-All, IIC-All, IIC-10th, and IFBC-10th) have lower time period. This indicates that, as the number of connected floors increase, the time period decreases. It means that by coupling beams in any floor levels, dynamic behavior of SBI system can be adjusted. This expression indicates that the dynamic behavior of SBI structure such as time period can be drastically adjusted by adding or removing coupling beams at various floor levels.
- (6) Time-history analysis with representative Northridge-01, 1994 (no. 14) ground motion data was used to compare the seismic responses of prototype buildings. Results showed that the response of IFBC-All

subjected to Northridge-01 is very close to IIC-All in terms of maximum absolute roof acceleration and maximum absolute roof displacement. Finally, it is concluded that in SBI system, when inner core is connected to the outer frame only at the top (e.g., model IIC-10th), results show that model IIC-10th has substantially reduced displacement, while acceleration and base shear could not be reduced with the increase of the stiffness of the structure caused by connecting the topmost floor to the outer frames, when compared to that of the IIC model. In contrast to models IFBC-10th, IFBC-All, IIC-All, and IFBC, model IIC-10th has both acceleration and base shear reduced.

- (7) According to the results obtained from model IIC-All, base isolation devices in double-skin SBI structure with all connected floor levels have somewhat trivial efficiency. Moreover, results show that the model IIC-10th exhibits a higher probability of collapse. Therefore, a model configuration of SBI system between models IIC-All and IIC-10th with for example two connected floor levels can be appropriate.
- (8) Double-skin SBI system was found to be effective in reducing the time period and displacement in conventional isolated structure with long time period and large displacement. Results reveal that by increasing or reducing the number of connected floors in the SBI system, dynamic behaviors of the SBI system can be changed. Therefore, an adjustable structure can be created by using coupling beams at every floor level. As stated earlier, the SBI system can provide significant structural integrity by transferring the lateral force resisting system (LFRS) from the inner core (isolated structure) to the outer frames with fixed base by eliminating the tensile forces (uplift) from LFRS which can cause instability in isolation devices.

## Conflicts of Interest

The authors declare no conflicts of interest.

## Authors' Contributions

All the authors made contributions to writing, revising, and proofreading the manuscript.

## Acknowledgments

The authors wish to acknowledge the supports of the National Natural Science Foundation of China (NSFC) (Grant nos. 51048001 and 51178264) and National Railway Ministry of China (Grant no. J2011G003).

## References

- [1] A. K. Chopra, *Dynamics of Structures: Theory and Applications to Earthquake Engineering*, Prentice-Hall, Upper Saddle River, NJ, USA, 2001.

- [2] B. S. Taranath, *Wind and Earthquake Resistant Buildings: Structural Analysis and Design*, CRC Press, Boca Raton, FL, USA, 2004.
- [3] T. K. Datta, *Seismic Analysis of Structures*, John Wiley & Sons, Hoboken, NJ, USA, 2010.
- [4] R. S. Jangid and T. K. Datta, "Nonlinear response of torsionally coupled base isolated structure," *Journal of Structural Engineering*, vol. 120, no. 1, pp. 1–22, 1994.
- [5] S. Nagarajaiah, A. M. Reinhorn, and M. C. Constantinou, "Torsion in base-isolated structures with elastomeric isolation systems," *Journal of Structural Engineering*, vol. 119, no. 10, pp. 2932–2951, 1993.
- [6] Z. Zhou, J. Wong, and S. Mahin, "Potentiality of using vertical and three-dimensional isolation systems in nuclear structures," *Nuclear Engineering and Technology*, vol. 48, no. 5, pp. 1237–1251, 2016.
- [7] O. Takahashi, H. Aida, J. Suhara, R. Matsumoto, Y. Tsuyuki, and T. Fujita, "Construction of civil building using three dimensional seismic isolation system: part 1, design of building using three dimensional seismic isolation system," in *Proceedings of the 14th World Conference on Earthquake Engineering*, Beijing, China, October 2008.
- [8] M. Morishita, S. Kitamura, S. Moro, Y. Kamishima, and T. Somaki, "Study on 3-dimensional seismic isolation system for next generation nuclear power plant—vertical component isolation system with coned disk spring," in *Proceedings of the 13th World Conference on Earthquake Engineering*, Vancouver, BC, Canada, August 2004.
- [9] S. Ogiso, "Development of 3D seismic isolator using metallic bellows," in *Transactions of the 17th International Conference on Structural Mechanics in Reactor Technology*, Prague, Czech Republic, August 2003.
- [10] K. Inoue, M. Fushimi, S. Moro, M. Morishita, S. Kitamura, and T. Fujita, "Development of three-dimensional seismic isolation system for next generation nuclear power plant," in *Proceedings of the 13th World Conference on Earthquake Engineering*, Vancouver, BC, Canada, August 2004.
- [11] T. Somaki, *Development of 3-Dimensional Base Isolation System for Nuclear Power Plants*, SMIRT, Washington, DC, USA, 2001.
- [12] J. Wong, Z. Zhou, and S. Mahin, *Seismic Isolation of Nuclear Power Plants*, Tech. Rep. 3002000561, Electric Power Research Institute Inc., Palo Alto, CA, USA, 2013.
- [13] J. Marko, *Influence of Damping Systems on Building Structures Subject to Seismic Effects*, Ph.D. thesis, School of Civil Engineering, Physical Infrastructure Center, Queensland University of Technology, Brisbane, Australia, 2006.
- [14] C. Bedon and C. Amadio, "Numerical assessment of vibration control systems for multi-hazard design and mitigation of glass curtain walls," *Journal of Building Engineering*, vol. 15, pp. 1–13, 2018.
- [15] C. Bedon and C. Amadio, "Enhancement of the seismic performance of multi-storey buildings by means of dissipative glazing curtain walls," *Engineering Structures*, vol. 152, pp. 320–334, 2017.
- [16] C. Bedon and C. Amadio, "Passive control systems for the blast enhancement of glazing curtain walls under explosive loads," *Open Civil Engineering Journal*, vol. 11, no. 1, pp. 396–419, 2017.
- [17] C. Amadio and C. Bedon, "Viscoelastic spider connectors for the mitigation of cable-supported façades subjected to air blast loading," *Engineering Structures*, vol. 42, pp. 190–200, 2012.
- [18] C. Bedon and C. Amadio, "Exploratory numerical analysis of two-way straight cable-net façades subjected to air blast loads," *Engineering Structures*, vol. 79, pp. 276–289, 2014.
- [19] P. C. Wong, D. Prasad, and M. Behnia, "A new type of double-skin façade configuration for the hot and humid climate," *Energy and Buildings*, vol. 40, no. 10, pp. 1941–1945, 2008.
- [20] S. Chou, K. Chua, and J. Ho, "A study on the effects of double skin façades on the energy management in buildings," *Energy Conversion and Management*, vol. 50, no. 9, pp. 2275–2281, 2009.
- [21] D.-W. Kim and C.-S. Park, "Difficulties and limitations in performance simulation of a double skin façade with EnergyPlus," *Energy and Buildings*, vol. 43, no. 12, pp. 3635–3645, 2011.
- [22] K. S. Moon, "Tall building motion control using double skin façades," *Journal of Architectural Engineering*, vol. 15, no. 3, pp. 84–90, 2009.
- [23] K. S. Moon, "Structural design of double skin facades as damping devices for tall buildings," *Procedia Engineering*, vol. 14, pp. 1351–1358, 2011.
- [24] G. Pipitone, G. Barone, and A. Palmeri, "Optimal design of double-skin façades as vibration absorbers," *Structural Control and Health Monitoring*, vol. 25, no. 2, p. e2086, 2018.
- [25] T. S. Fu and R. Zhang, "Integrating double-skin façades and mass dampers for structural safety and energy efficiency," *Journal of Architectural Engineering*, vol. 22, no. 4, p. 04016014, 2016.
- [26] G. Barone, A. Palmeri, and A. Khetawat, "Passive control of building structures using double-skin façades as vibration absorbers," in *Proceedings of the Fifteenth International Conference on Civil, Structural and Environmental Engineering Computing*, Prague, Czech Republic, September 2015.
- [27] S. Mazzoni, F. McKenna, M. H. Scott et al., *OpenSees Command Language Manual*, University of California, Berkley, MI, USA, 2007.
- [28] *Uniform Building Code, (UBC-97), Part. 2*, 1997.
- [29] ACI Committee, AC Institute, and I.O.f. Standardization, *Building Code Requirements for Structural Concrete (ACI 318-11) and Commentary*, American Concrete Institute, Farmington Hills, MI, USA, 2011.
- [30] I. D. Karsan and J. O. Jirsa, "Behavior of concrete under compressive loadings," *Journal of the Structural Division*, vol. 95, no. 12, pp. 2543–2563, 1969.
- [31] C. Providakis, "Effect of LRB isolators and supplemental viscous dampers on seismic isolated buildings under near-fault excitations," *Engineering Structures*, vol. 30, no. 5, pp. 1187–1198, 2008.
- [32] R. S. Jangid, "Optimum lead-rubber isolation bearings for near-fault motions," *Engineering Structures*, vol. 29, no. 10, pp. 2503–2513, 2007.
- [33] R. Han, Y. Li, and J. van de Lindt, "Seismic risk of base isolated non-ductile reinforced concrete buildings considering uncertainties and mainshock-aftershock sequences," *Structural Safety*, vol. 50, pp. 39–56, 2014.
- [34] V. Kilar and D. Koren, "Seismic behaviour of asymmetric base isolated structures with various distributions of isolators," *Engineering Structures*, vol. 31, no. 4, pp. 910–921, 2009.
- [35] E. Kalkan and A. K. Chopra, "Evaluation of modal pushover-based scaling of one component of ground motion: tall buildings," *Earthquake Spectra*, vol. 28, no. 4, pp. 1469–1493, 2012.
- [36] M. Fairhurst, X. Zhang, and T. Tannert, "Nonlinear dynamic analysis of a novel timber-steel hybrid system," in *Proceedings of the World Conference on Timber Engineering*, Quebec City, QC, Canada, August 2014.

- [37] A. Masroor and G. Mosqueda, *Seismic Response of Base Isolated Buildings Considering Pounding to Moat Walls*, MCEER, 2013.
- [38] C. Bedon and A. Morassi, "Dynamic testing and parameter identification of a base-isolated bridge," *Engineering Structures*, vol. 60, pp. 85–99, 2014.
- [39] F. Naeim and J. M. Kelly, *Design of Seismic Isolated Structures: from Theory to Practice*, John Wiley & Sons, New York, NY, USA, 1999.
- [40] T. K. Datta, *Seismic Analysis of Structures*, Indian Institute of Technology, John Wiley & Sons (Asia) Pte Ltd., Delhi, India, 1994.
- [41] O. Gomase and S. Bakre, "Performance of non-linear elastomeric base-isolated building structure," *International Journal of Civil and Structural Engineering*, vol. 2, no. 1, p. 280, 2011.
- [42] A. Tena-Colunga and C. Zambrana-Rojas, "Dynamic torsional amplifications of base-isolated structures with an eccentric isolation system," *Engineering Structures*, vol. 28, no. 1, pp. 72–83, 2006.
- [43] A. Tena-Colunga and J. L. Escamilla-Cruz, "Torsional amplifications in asymmetric base-isolated structures," *Engineering Structures*, vol. 29, no. 2, pp. 237–247, 2007.
- [44] C. P. Providakis, "Pushover analysis of base-isolated steel-concrete composite structures under near-fault excitations," *Soil Dynamics and Earthquake Engineering*, vol. 28, no. 4, pp. 293–304, 2008.
- [45] R. Tyler and W. Robinson, "High-strain tests on lead-rubber bearings for earthquake loadings," *Earthquake Engineering*, vol. 17, no. 2, 1984.
- [46] H. C. Tsai, "Dynamic analysis of base-isolated shear beams bumping against stops," *Earthquake Engineering & Structural Dynamics*, vol. 26, no. 5, pp. 515–528, 1997.
- [47] J. Chen, C. Zhao, Q. Xu, and C. Yuan, "Seismic analysis and evaluation of the base isolation system in AP1000 NI under SSE loading," *Nuclear Engineering and Design*, vol. 278, pp. 117–133, 2014.
- [48] E. N. Dvorkin, D. Pantuso, and E. A. Repetto, "A formulation of the MITC4 shell element for finite strain elasto-plastic analysis," *Computer Methods in Applied Mechanics and Engineering*, vol. 125, no. 1–4, pp. 17–40, 1995.
- [49] X. Lu, L. Xie, H. Guan, Y. Huang, and X. Lu, "A shear wall element for nonlinear seismic analysis of super-tall buildings using OpenSees," *Finite Elements in Analysis and Design*, vol. 98, pp. 14–25, 2015.
- [50] L. Xie, X. Lu, X. Lu, Y. Huang, and L. Ye, "Multi-layer shell element for shear walls in OpenSees," *Computing in Civil and Building Engineering*, pp. 1190–1197, 2014.
- [51] The Pacific Earthquake Engineering Research Center, *PEER Database*, University of California, Berkeley, CA, USA, 2013.
- [52] M. S. Zadeh and M. S. Saiidi, *Pre-Test Analytical Studies of NEESR-SG 4-Span Bridge Model Using OpenSees*, Tech. Rep. CCEER-07, University of Nevada, Reno, NV, USA, 2007.
- [53] P. Jehel, P. Léger, and A. Ibrahimbegovic, "Initial versus tangent stiffness-based Rayleigh damping in inelastic time history seismic analyses," *Earthquake Engineering & Structural Dynamics*, vol. 43, no. 3, pp. 467–484, 2014.
- [54] FEMA P695, *Quantification of Building Seismic Performance Factors*, Federal Emergency Management Agency, Washington, DC, USA, 2009.
- [55] Engineers, A.S.o.C., *Seismic Rehabilitation of Existing Buildings*, Vol. 41, ASCE Publications, Reston, VI, USA, 2007.
- [56] D. Vamvatsikos and C. A. Cornell, "Incremental dynamic analysis," *Earthquake Engineering & Structural Dynamics*, vol. 31, no. 3, pp. 491–514, 2002.
- [57] FEMA 350, *Recommended Seismic Design Criteria for New Steel Moment-Frame Buildings*, FEMA, Washington, DC, USA, 2000.
- [58] E. Dumova-Jovanoska, "Fragility curves for reinforced concrete structures in Skopje (Macedonia) region," *Soil Dynamics and Earthquake Engineering*, vol. 19, no. 6, pp. 455–466, 2000.
- [59] G. Altay, G. Deodatis, G. Franco et al., "Benefit-cost analysis for earthquake mitigation: evaluating measures for apartment houses in Turkey," in *Proceedings of the 2nd Annual IIASA-DPRI Meeting, Integrated Disaster Management*, Laxenburg, Austria, July 2002.
- [60] Federal Emergency Management Agency, *HAZUS-MH MR4 Earthquake Model Technical Manual*, Federal Emergency Management Agency, Washington, DC, USA, 2009.
- [61] M. S. Kirçil and Z. Polat, "Fragility analysis of mid-rise R/C frame buildings," *Engineering Structures*, vol. 28, no. 9, pp. 1335–1345, 2006.
- [62] D. Vamvatsikos, F. Jalayer, and C. A. Cornell, "Application of incremental dynamic analysis to an RC-structure," in *Proceedings of the FIB Symposium on Concrete Structures in Seismic Regions*, Athens, Greece, May 2003.
- [63] A. Gunduz, *Probability, Statistics, Risk and Reliability in Engineering*, Kure publications, Istanbul, Turkey, 1996.



**Hindawi**

Submit your manuscripts at  
[www.hindawi.com](http://www.hindawi.com)

